Multi-scale experimental testing on variable stiffness and damping components for semi-active structural control

Wang, Qinyu; Senatore, Gennaro; Jansen, Kaspar; Habraken, Arjan; Teuffel, Patrick

DOI
10.1016/j.compstruct.2021.114976

Publication date
2021

Document Version
Final published version

Published in
Composite Structures

Composite Structures 281 (2022) 114976

Contents lists available at ScienceDirect

Composite Structures

journal homepage: www.elsevier.com/locate/compstruct

Multi-scale experimental testing on variable stiffness and damping components for semi-active structural control

Qinyu Wang [a,*], Gennaro Senatore [b,*], Kaspar Jansen [c], Arjan Habraken [a], Patrick Teuffel [a]

[a] Chair of Innovative Structural Design, TU Eindhoven, Eindhoven, the Netherlands
[b] Applied Computing and Mechanics Laboratory, Swiss Federal Institute of Technology, Lausanne, Switzerland
[c] Department of Design Engineering, TU Delft, Delft, the Netherlands

ARTICLE INFO

Keywords:
Adaptive structures
Semi-active vibration control
Variable stiffness and damping
Structural joint
Viscoelastic material
Multiscale experimental testing

ABSTRACT

This paper presents experimental testing of a new semi-active vibration control device comprising a shape memory polymer (SMP) core that is reinforced by an SMP-aramid composite skin. This control device works as a load-transfer component that can be integrated into truss and frame structures in the form of a joint. At the material level, thermal actuation from ambient (25 °C) to transition temperature (65 °C) causes a significant 40-fold increase in damping due to viscoelastic effects. At the component level, uniaxial tensile and four-point bending tests have shown that tensile strength depends primarily on the bond strength between the reinforcement skin and the structural element while flexural strength depends on the strength of the reinforcement skin fibers. Through cyclic testing, it has been observed that material viscoelasticity is beneficial to ductility and energy dissipation. When the joint core is actuated to the SMP transition temperature, axial and flexural stiffness decrease by up to 50% and 90%, respectively. The property change at material and component levels enable tuning the frequency and damping ratio at the structure level, which has been successfully employed to mitigate the dynamic response of a 1/10 scale three-story prototype frame under resonance and earthquake loadings.

1. Introduction

1.1. Previous work

Integration of sensing and actuation technologies into structures enables new capabilities such as self-diagnosis, damage detection as well as to actively counteract the effect of loading through adaptation. Compared to passive structural systems, structures equipped with sensors and actuators can be designed to operate with better material utilization [1–2] and significantly reduced whole-life energy requirements [3–4]. Whole-life energy accounts for the share of energy (or carbon equivalent) embodied in the material and the operational share for active control. Numerical and experimental studies have shown that well-designed adaptive structures achieve savings up to 70% of the whole-life energy compared to passive structures, thus reducing adverse environmental impacts [5–7].

Implementation of vibration control measures is important to ensure the safety of buildings and bridges under dynamic excitations such as pedestrian and vehicular traffic, high winds, and earthquakes. Strong vibrations may cause failure and, generally, are likely to significantly reduce the structure service lifespan. Structural control strategies have been grouped into four categories: passive, active, semi-active, and hybrid [8–12]. Passive control systems require no input energy because control forces are developed through the motion of the structure. Typical passive systems are base isolation systems [13], viscoelastic and elastoplastic dampers [14], and passive mass dampers [15]. Generally, passive control systems have limited control capabilities compared to active and semi-active systems. Passive systems are effective to control the response if the structural characteristics do not change over time and the predicted loading conditions do no fluctuate too much, which is unlikely for most mechanical and civil engineering applications (e.g. typical building and bridge scenarios). When a change in the structural and/or environmental characteristics occurs, it might result in significant degradation of control performance which therefore poses a reliability issue. Active control devices, such as active tuned mass dampers [16] and bracing systems [17], provide control forces through actuation based on feedback from sensors that measure the structure response. Although these active devices perform significantly better than passive ones and are effective in a wide range of conditions, they typically require a high-power density supply and a complex control system [12].

* Corresponding authors.
E-mail addresses: q.wang2@tue.nl (Q. Wang), gennarosenatore@gmail.com (G. Senatore).

https://doi.org/10.1016/j.compstruct.2021.114976
Received 15 July 2021; Accepted 8 November 2021
Available online 13 November 2021

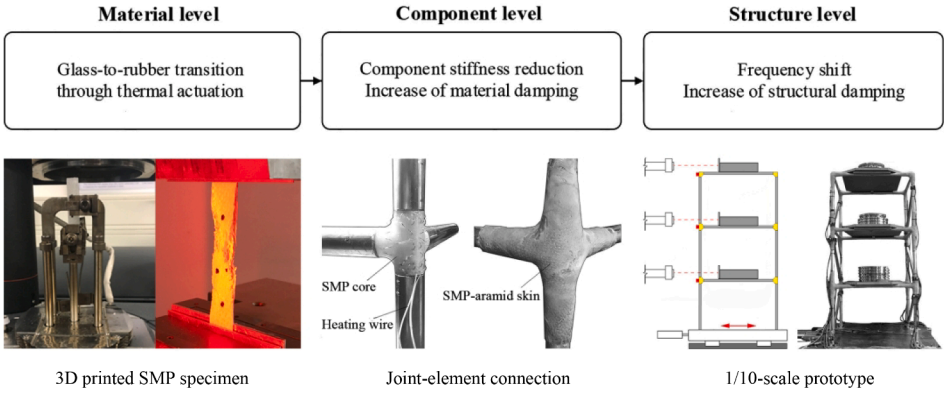

Fig. 1. Thermal actuation of adaptive joints: material, component, and structure.

Measurement and modeling inaccuracy might, in some cases, cause instability of the structure-control system [18]. Active solutions typically involve higher monetary costs in comparison to passive control systems. Semi-active systems, such as magnetorheological (MR) dampers as well as variable stiffness and damping devices, perform better than passive systems, are generally reliable and maintain some of the versatility and adaptability of fully active systems [19–20]. Semi-active systems require a smaller input power source for operation compared to active control devices since control forces are developed as a result of the movement of the structure. Hybrid control systems (e.g. hybrid mass dampers) might combine passive, active, and semi-active control strategies and devices [21–22]. Hybrid control systems can effectively control the dynamic response of buildings under a broad set of loading conditions. However, they are generally complex and might involve significant maintenance costs [23].

Semi-active strategies based on stiffness and damping control mitigate the structure response through adjusting the structural dynamic properties [24–26]. Existing stiffness and damping control systems comprise several parts and generally require complex detailing for installation. In addition, existing devices are effective within specific conditions such as limited yield displacements and they require damping provided by external means [25–26]. This work presents experimental testing of a new variable stiffness and damping control device consisting of a shape memory polymer core that is reinforced by an SMP-aramid composite skin. This new control device also functions as a load-transfer component [27], which enables seamless integration into structures. The new variable stiffness and damping control device investigated in this work is in the form of a joint for frame and truss structures and is referred to as "adaptive joint" (or adaptive component) hereafter. Compared to existing variable stiffness and damping solutions for vibration control, adaptive components are simpler because they do not involve complex mechanisms based on moving parts since they are controlled through thermal actuation (solid-state). The actuation mechanism is inherent within the properties of the material enabling a reliable control system that is able to perform optimally for diverse structural systems (e.g. multi-story buildings, bridges, airplane wings, wind turbine blades, etc.) [28].

1.2. New contribution

This paper describes multi-scale experimental studies on variable stiffness and damping adaptive components for vibration control. New contributions are:

- This work links experimental studies at the material, component and structural levels.
- A new shake table test under Northridge earthquake is performed on a 1/10 scale three-story frame prototype equipped with 12 adaptive joints. Results are compared with those obtained under El Centro earthquake that was tested in previous work [29].
- Component-level testing is carried out to investigate strength and stiffness characteristics of the joint-element connection. Experimental results provide important insights to improve the design of the joint-element assembly.

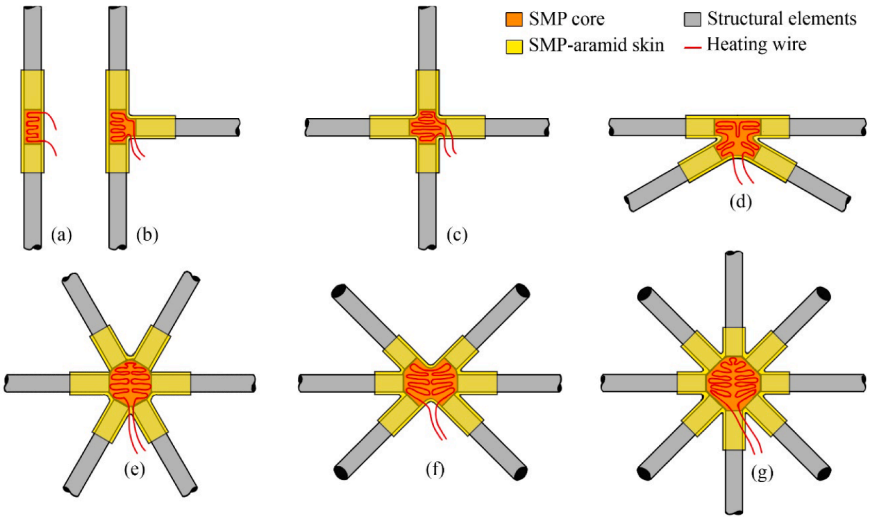

Fig. 2. SMP structural joint connected to (a) two, (b) three, (c-d) four, (e-f) six, and (g) eight elements.

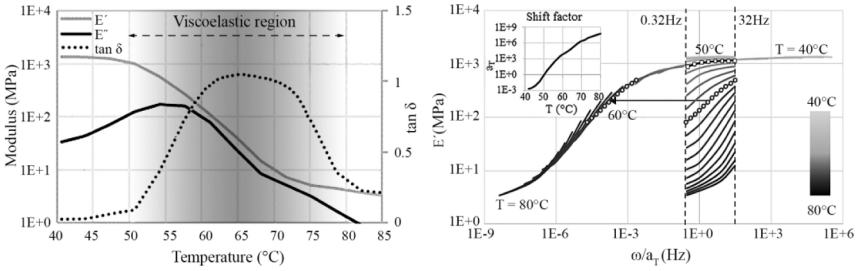

Fig. 3. SMP material characterization through DMA: (a) storage modulus (E'), loss modulus (E''), and material damping (tan δ) vs. temperature at 1 Hz; (b) master curve [27].

1.3. Outline

This paper is arranged into six sections. Experimental studies have been carried out at three scale levels: material, component, and structure. Section 2 describes material- and structure-level testing. Component-level testing is described in Sections 3 and 4. Mechanical properties of the connection between adaptive joint and structural elements are characterized through tensile and bending testing under monotonic and cycling loading. Section 5 offers a discussion about the interconnection between results obtained at material-, component- and structure-level testing. Section 6 concludes this paper.

2. Three-scale level testing: material, component, and structure

An adaptive joint comprises a shape memory polymer (SMP) core reinforced by an SMP-aramid composite skin. At the material level, thermal actuation of the SMP core causes a large stiffness reduction and a significant increase of damping due to viscoelastic effects. At the component level, the flexural stiffness of the joint-element connection decreases significantly, which can be thought of as a transition from a moment-resisting to a pin connection. The property change at material and component levels enable tuning frequency and damping ratio at the structure level, which has been employed as a semi-active control strategy to mitigate the response under dynamic excitations [28–29]. The multi-scale effect of thermal actuation of adaptive components is illustrated in the flowchart of Fig. 1.

The adaptive joint has been designed to be easily connected to structural elements. An example with elements having a hollow circular cross-section is given in Fig. 2, which shows the joint connected to 2, 3, 4, 6, and 8 elements. Since SMP is a suitable material for additive manufacturing (i.e. 3D printing), the geometry of the adaptive joint core can be easily modified to connect with multiple elements having any type of cross-section.

An experimental investigation has been implemented at the material, component and structure level. At the material level, dynamic mechanical analysis (DMA) has been carried out to characterize the thermomechanical properties of 3D-printed SMP, SMP resin, and SMP fiber-reinforced composite specimens. At the component level, the capacity and stiffness of the connections between adaptive joints with structural elements have been investigated through uniaxial tensile and four-point bending tests under monotonic and cycling loading. At the structure level, shake table tests have been carried out on a 1/10 scale three-story frame prototype equipped with twelve adaptive joints.

2.1. Material-level tests: characterization of joint core and skin materials

2.1.1. Material model of joint core: thermoelastic and viscoelastic

Shape memory polymers (SMPs) can recover their original shape in stress-free conditions from a deformed state through thermal actuation [30] which causes a transition from a glassy to a rubbery state. During the transition phase, there is a significant reduction of stiffness and an increase of damping. Typically, below transition temperature T_g, the polymer is relatively stiff with a modulus of approximately 1 GPa whereas, above T_g, the polymer has a rubbery elastic behavior with a modulus that can reduce from 100 to 10,000 times [31]. Above the glass transition temperature T_g, the polymer chain segments between cross-links can deform freely which allows large macroscopic strains (up to 400%) [32].

The thermomechanical properties of the SMP joint core material (MM5520, *SMP Technologies Inc.*) have been characterized through dynamic mechanical analysis (DMA) tests in [27]. Fig. 3a shows the plots of storage modulus E', loss modulus E'' and tan δ as functions of the temperature at a strain rate of 1 Hz. The storage modulus characterizes the elastic behavior in either the glassy or rubbery state (strain and stress are in phase). When the material enters the viscoelastic region, strain and stress go out of phase. Energy dissipation through heating due to friction is characterized by the loss modulus E''. The ratio $\tan\delta = E''/E'$ is a measure of damping [33–34]. The transition temperature T_g is 65 °C, which is the temperature at which the material damping reaches the maximum. Note that during state transition (50 °C to 65 °C), the modulus drops from 1340 MPa to 37 MPa. The elastic stiffness reduces by 96% while damping increases 11 times. Two material models have been developed through DMA: thermo-elastic and viscoelastic [27]. The thermo-elastic model is a simplified material model, which takes the storage modulus curve at 1 Hz, shown in Fig. 3a while ignoring damping variation caused by viscoelastic effects. The viscoelastic material model instead characterizes stiffness and damping variation with temperature and strain rate (i.e. frequency). The time–temperature superposition principle has been applied to map experimental data obtained at different temperatures and frequencies onto a single master curve, which is shown in Fig. 3b.

When the joints are thermally actuated, the structure's natural frequency shifts. This is caused primarily by the joint stiffness reduction and thus viscoelastic effects can be neglected. For this reason, the thermo-elastic model is employed in modal analysis to evaluate the structure's natural frequency shift with temperature and to analyze the dynamic response for the uncontrolled case (at 25 °C the joint core material is elastic). The viscoelastic material model is employed to analyze the dynamic response in the temperature range 40 °C to 65 °C.

2.1.2. SMP-aramid skin: isotropic elastic material model

SMPs are often manufactured as composite materials to improve their mechanical properties which are typically characterized by low stiffness and recovery stress. SMP composites (SMPC) have been used in biomedical applications, solid-state actuators and smart textiles [35–36]. SMPCs are often integrated with continuous fibers (e.g., carbon, glass and aramid) which increase mechanical strength and stiffness in the fiber (axial) direction while the shape memory effect is retained in the transverse direction [37]. Continuous fiber-reinforced SMPCs are more resistant to impact, crash and fatigue and thus are more suitable to be employed in structural applications [36–37].

The SMP-aramid skin that is part of the adaptive joint system has two

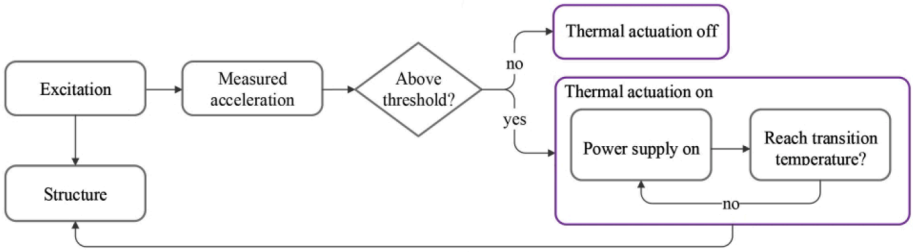

Fig. 4. Semi-active vibration control strategy flow-chart [28].

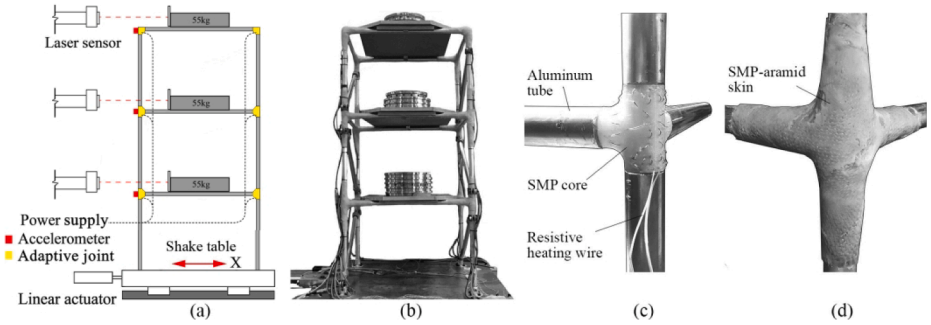

Fig. 5. (a) Experimental setup; (b) three-story adaptive frame prototype; (c) SMP core connected to four aluminum tubes; (d) SMP-aramid skin.

functions: to limit deformations under loading when the joint core stiffness is reduced through thermal actuation and to strengthen the connection of the joint with structural elements. The skin consists of a stack of woven aramid (Kevlar) fabric layers which are impregnated with SMP material to form a stiff and thin composite. The individual fabric layers have fibers oriented at 0° and 90°, resulting in a large degree of anisotropy. Since joints for spatial structures are generally expected to take tensile, bending and torsional forces, two fabric layers with 45° orientation are sandwiched between the two layers with 0°/90° fiber orientation resulting in a quasi-isotropic skin with a modulus of approximately 8320 MPa and a thickness of 1.72 mm [27]. Thicker skins may be needed to prevent excessive deformation of the joint core if stronger loads are applied. In that case, additional 0° and 45° layers can be added.

2.2. Structure-level tests: shake table test on a three-story frame

2.2.1. Semi-active feedforward control

For structures equipped with adaptive joints, the change of material properties that occurs in the transition phase triggered by thermal actuation induces a shift of natural frequencies and an increase of the damping ratio. Numerical simulations have shown that such frequency shift and damping increment can be effectively employed to mitigate the structure response under dynamic excitation. Under excitations that have several high-energy frequency components (e.g. earthquakes), although a temporary resonance condition may occur in some cases due to the structure frequency shift, the effect of damping increment is dominant when the joints are actuated to the transition temperature [28]. A simple feedforward control scheme has been proposed to mitigate the structural response through thermal actuation of the joints. Fig. 4 shows the control strategy flow-chart for seismic response control. After detecting the excitation (ground acceleration), the joints are actuated to the transition temperature. Thermal actuation is switched off when a control stop criterion is met, for example, the ground acceleration reduces below a set threshold. The joints are cooled down to the field temperature through natural or forced ventilation.

Table 1
Three-story frame prototype: frequency and damping variation for 1st and 2nd modes.

	25 °C	40 °C	45 °C	50 °C	55 °C	60 °C	65 °C
ω_1^e (Hz)	3.34	2.88	2.77	2.57	2.43	2.32	2.1
ω_2^e (Hz)	10.96	9.63	9.32	9.08	8.84	8.23	7.54
$S_{\omega 1}^e$ (%)	–	13.8	17.1	23.1	27.2	30.5	37.1
$S_{\omega 2}^e$ (%)	–	12.1	15.0	17.2	19.3	24.9	31.2
ζ^e (%)	2.6	4.4	5.3	6.4	8.0	9.4	11.3

2.2.2. 1/10 scale three-story frame prototype

Shake table tests have been carried out on a 650 mm × 650 mm × 1325 mm three-story frame prototype that is shown in Fig. 5a and b. The structure has been designed to take a dead load of 150 kg/m^2 which is equivalent to 55 kg mass applied on each floor. The core of the joints has been manufactured through fused deposition modeling (i.e. 3D printing). Each joint is connected to either three or four aluminum tube elements. The joint core features 50 mm long extensions that are fitted inside the tube elements and held in position via structural glue, Fig. 5c. The SMP-aramid reinforcement skin is then applied to complete the joint-element assembly as shown in Fig. 5d.

A data acquisition system (cDAC-9178, National Instruments) is employed to monitor the structure response. The acceleration and displacement of each floor are measured by an accelerometer (BDK3 from *seika.de*®) and a laser sensor (M5L-200 from MEL Mikroelektronik GmbH), respectively. A real-time target machine (NI cRIO-9038, National Instruments) is employed to control the shake table motion through a linear actuator (T60, *Thomson*) and to modulate the power supply for thermal actuation of the joints, which is provided by two power supplies (230 V/12VDC, 350 W, *Schloss*). Thermal actuation is implemented using a resistive heating wire that is passed through a series of holes obtained by means of selective deposition. Twelve solid-state relays (DC60S5, *Crydom*) are employed to control independently the power supply to the heating wire embedded in each joint. The thermal flux is regulated through a resistance temperature detector (RTD) (F2020-100-A, Omega) that is installed on each heating wire. The surface temperature of each joint is monitored with a thermocouple and it is recorded through a multi-channel data logger (Squirrel 2040, *Grant*).

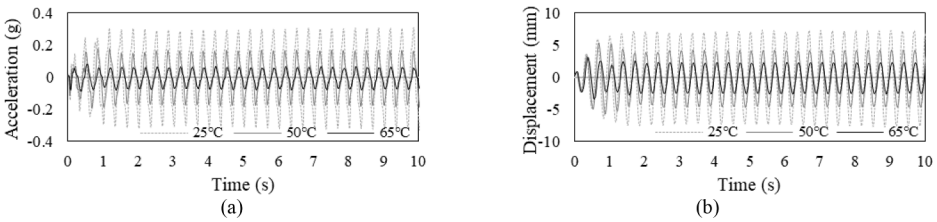

Fig. 6. 1/10-scale prototype: top-story (a) absolute acceleration and (b) relative displacement response time history under sinusoidal base excitation at 25 °C, 50 °C, and 65 °C.

Table 2
Seismic response control under El Centro and Northridge: uncontrolled (25 °C) vs controlled (65 °C).

Earthquake		El Centro		Northridge	
		Uncontrolled (25 °C)	Controlled (65 °C)	Uncontrolled (25 °C)	Controlled (65 °C)
Peak displacement(mm)	1S	4.83	4.03	6.31	4.72
	2S	10.02	9.49	7.42	8.71
	3S	13.35	13.685	6.09	6.68
Peak drift ratio	1S&2S	0.0119	0.0145	0.0083	0.0128
	2S&3S	0.0096	0.0115	0.0110	0.0123
Peak acceleration (g)	1S	0.32	0.40	0.58	0.36
	2S	0.54	0.37	0.62	0.49
	3S	0.81	0.41	1.03	0.47
Peak base shear (kN)		0.51	0.27	1.06	0.35
Normed displacement(mm)	1S	1.02	0.71	1.08	0.97
	2S	2.18	0.87	1.37	1.89
	3S	3.04	0.96	1.01	1.47
Normed drift ratio	1S&2S	0.0028	0.0031	0.0016	0.0029
	2S&3S	0.0027	0.0030	0.0021	0.0027
Normed acceleration (g)	1S	0.071	0.066	0.093	0.079
	2S	0.108	0.066	0.112	0.081
	3S	0.146	0.072	0.164	0.091
Normed base shear (kN)		0.099	0.058	0.170	0.069

2.2.3. *Frequency shift and damping ratio variation measurement*

Frequency shift and damping variation caused by thermal actuation of the joints are measured through free vibration tests. A 20 mm base displacement is applied through the shake table. Natural frequency and frequency shift for 1st and 2nd modes are given in Table 1. The modal frequencies are obtained through Fast Fourier Transform (FFTs) of the recorded acceleration. The 1st and 2nd mode frequency shifts from ambient (25 °C) to transition temperature (65 °C) are 37.1% (from 3.34 Hz to 2.1 Hz) and 31.2% (from 10.96 Hz to 7.54 Hz), respectively. The logarithmic decrement method is applied to compute the damping ratio variation that is given in Table 1. The increase of material damping due to viscoelastic effects results in a 4.3-fold increase of the structural damping ratio from ambient (2.6%) to transition temperature (11.3%).

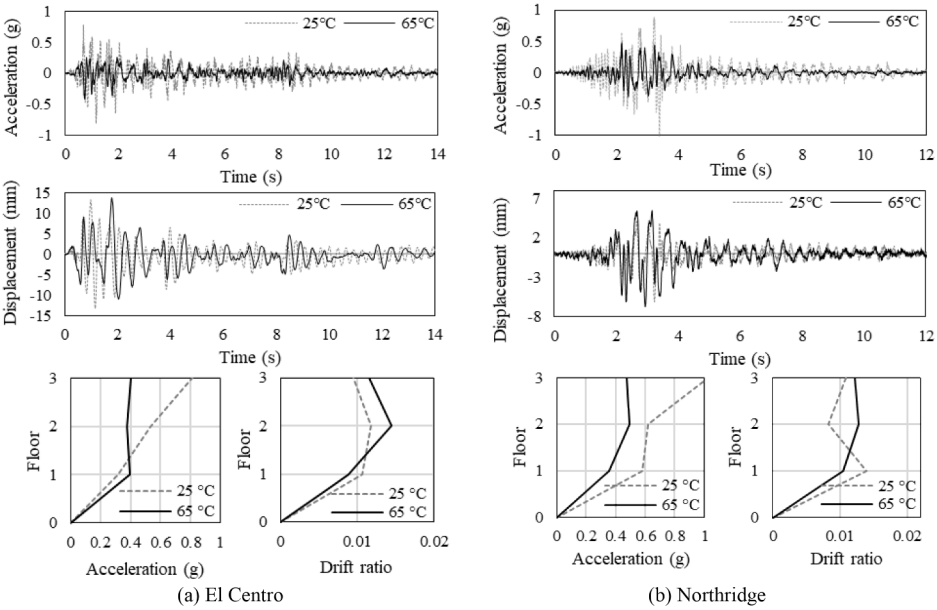

Fig. 7. 1/10-scale prototype: top-story absolute acceleration and relative displacement response time history under (a) El Centro and (b) Northridge base excitations for uncontrolled (25 °C) and controlled (65 °C) cases.

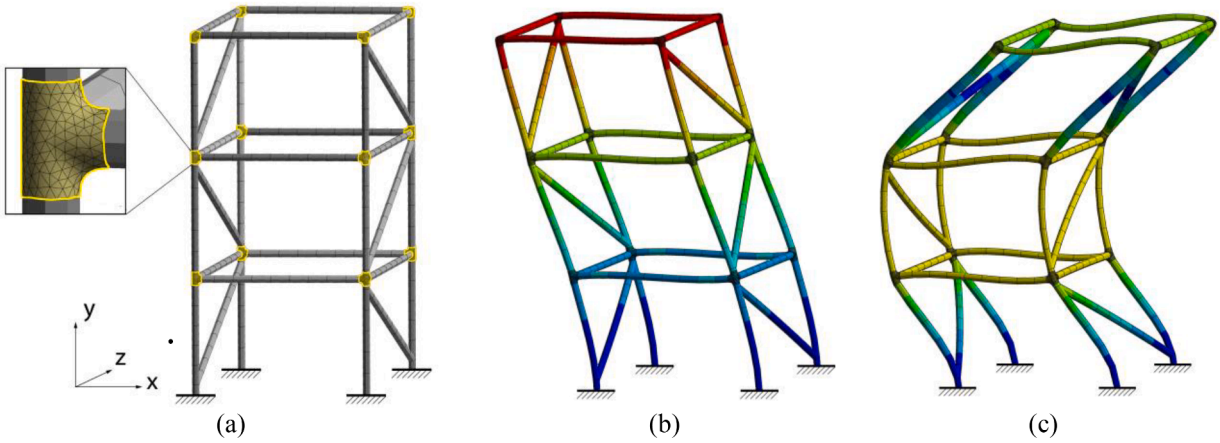

Fig. 8. (a) FEM model with joint mesh close-up; 1st (b) and 2nd (c) modal shapes.

2.2.4. Response control under harmonic load

Control performances are first evaluated under a sinusoidal ground motion. The base excitation has a frequency of 3.0 Hz, an amplitude of 1 mm and it is applied for a period of 10 s. Although the 1st modal frequency has been recorded as 3.34 Hz, it was found that the 1st mode is excited when the base excitation frequency is set to 3.0 Hz. This difference might be caused by connection looseness between diagonal bracings and columns as well as between the frame structure and the shaking table. Fig. 6 shows the top-story acceleration and displacement responses for the uncontrolled case (25 °C), and when the joints are actuated to 50 °C and 65 °C, respectively. Top-story acceleration, top-story displacement, and base shear are reduced by up to 76% (from 0.324 to 0.079 g), 66% (from 7.7 to 2.63 mm), and 85% (from 0.34 to 0.05kN) respectively.

2.2.5. Response control under earthquake

A shake table test is performed under Northridge earthquake. Results are compared with those obtained under El Centro earthquake that was tested in previous work [29]. Table 2 gives peak and normed displacement, drift ratio, acceleration and base shear for all stories throughout the duration of the excitation. The story level is indicated by #S. Response values are given for the uncontrolled case (25 °C) when the joints are kept at ambient temperature as well as the controlled case (25 °C) when the joints are actuated to 65 °C. Fig. 7 shows the top-story acceleration and displacement responses as well as the acceleration and interstory drift ratio profiles over the structure height for the uncontrolled (25 °C) and controlled case (65 °C).

Control performance in terms of acceleration and base shear reduction under El Centro and Northridge earthquakes, respectively, are:

- The top story peak acceleration is reduced by up to 50% (from 0.81 to 0.41 g) and 54% (from 1.03 to 0.47 g)
- The normed acceleration is reduced by up to 50% (from 0.146 to 0.072 g) and 45% (from 0.164 to 0.091 g)
- Base shear is reduced by up to 47% (from 0.51 to 0.27kN) and 67% (from 1.06 to 0.35kN)
- The normed base shear is reduced by up to 41% (from 0.099 to 0.058kN) and 60% (from 0.170 to 0.069kN)

Since the structure becomes more flexible, an increase in displacement and interstory drift occurs which, however, is kept within the limits recommended by ASCE7-10. Shake table tests have confirmed that seismic response control through thermal actuation of adaptive joints is effective under different earthquake excitations.

2.2.6. Effect of control time delays on performance

In all experiments described so far, the joints have been thermally actuated from ambient (25 °C) to transition temperature T_g (65 °C) in discrete steps. Sufficient time has been allowed for the joint temperature to stabilize at the set value before applying the base excitation. The thermal actuation system has been sized to operate at low power in order to prevent potential damage caused by burns. For this reason, the effect of control time delays has been evaluated through simulations by means of full transient analysis and using the viscoelastic material model derived through DMA. The structural model has been appropriately scaled up from 1/10 to 1/1 using Cauchy and Groude similitude laws. The structure has been discretized through finite elements in Ansys Workbench. The columns and story beams are modeled with beam elements, the joints through solid elements, and the reinforcement skin through shell elements. Fig. 8 shows the FEM model in (a) as well as the

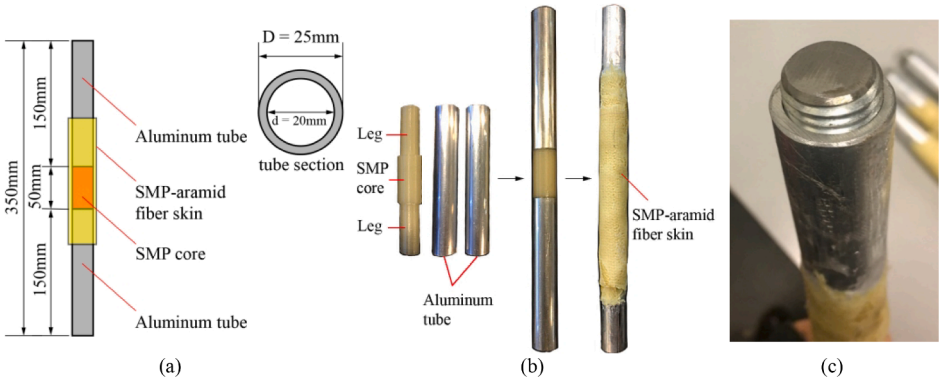

Fig. 9. SMP structural joint test specimens: (a) specimen dimensions; (b) specimen assembly; (c) specimen end fitted for clamping.

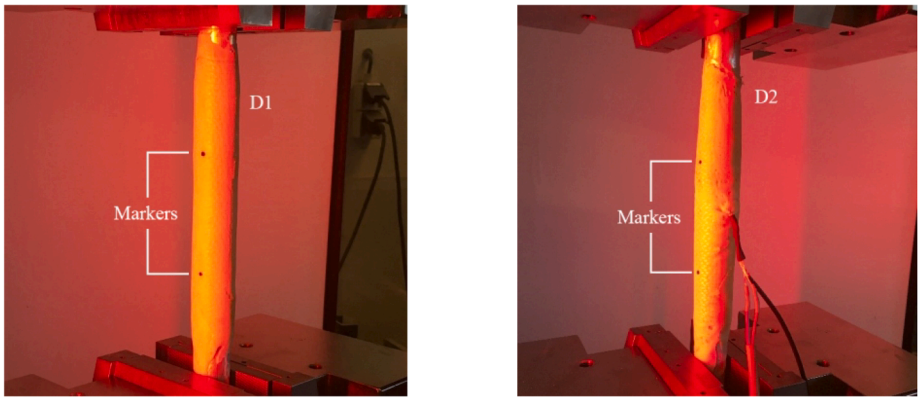

Fig. 10. Tensile test setup for (a) monotonic and cyclic test at 25 °C (D1) and cyclic test at 65 °C (D2).

1st and 2nd mode shapes in (b) and (c), respectively.

The thermal actuation system is assumed to be able to increase the joint temperature from ambient to transition within 8 s with a heating rate of 5 °C/s. Simulations under several earthquake loadings have shown that vibration suppression starts to be effective as the joints enter the visco-elastic region (in this case after 5 s). In cases where the ground acceleration reaches the maximum value after the cores of the joints are actuated to the transition temperature, control performance does not degrade. However, if the joints cores temperature reaches the transition value after the ground acceleration peaks, control performance is negatively affected. The reader is referred to [29] for further information regarding shake table tests of the 1/10 scale prototype as well as the effect of control time delays.

Control time delays can be drastically reduced by choosing an SMP with a lower transition temperature. There exist SMP with transition temperature that varies in the range 10 °C to 178 °C [38]. Generally, the SMP type should be chosen to minimize time delays due to heating as well as interference with field temperature. Control time delays can be further reduced by designing a more efficient thermal actuation system. For example, by embedding conductive materials in the reinforcement skin or through inducting heating by mixing magnetic particles with the joint core resin.

3. Monotonic and cyclic tensile test on joint-element connection

3.1. Test specimen

Monotonic and cyclic bending tests are carried out to evaluate the mechanical properties of the joint-element connection that has been employed for structure-level testing of the 1/10 scale frame prototype (Section 2.2). For simplicity, tests are carried out on a cylindrical specimen, shown in Fig. 9a. The core is fabricated through fused deposition modeling. The filament used for 3D printing is made of a polyurethane-based shape memory polymer MM5520 (SMP Technologies Inc., Tokyo, Japan). A transition temperature of 65 °C has been obtained from the 1 Hz tan delta peak measured through DMA on 3D-printed specimens [27]. This SMP is identical to that used to fabricate the joints described in Section 2. A 1 mm diameter resistive heating wire wrapped with an insulating layer is passed through the joint core via a series of holes that have been made by means of selective deposition. The 3D printed cylinder core has a diameter of 25 mm and a length of 50 mm. The joint core comprises two 50 mm long extensions, shown in Fig. 9b, that are called "legs" for brevity. The legs have a diameter of 20 mm to fit inside two aluminum tube elements having an outer diameter of 25 mm. The tube elements have a length of 150 mm and are fixed to the joint core using structural glue (Pattex® 100%). Four layers of aramid fiber cloths are then applied onto the joint-element connection and impregnated with SMP resin. After the resin is fully cured (24 h at ambient temperature), the SMP-aramid composite attaches firmly thereby completing the joint-element connection. The assembly of the specimen is shown in Fig. 9b. To avoid potential damage during testing, a short cylinder rod fitted in the tube elements is employed for clamping, as shown in Fig. 9c.

Monotonic tensile and bending tests are carried out at ambient temperature (25 °C) to set a reference with regard to stiffness and strength properties. Cyclic tensile and bending tests are carried out at ambient temperature as well as by thermally actuating the core to the transition temperature in order to evaluate the properties of the joint element-connection for the uncontrolled (25 °C) and controlled case (65 °C), respectively.

3.2. Monotonic uniaxial tensile test (25 °C)

3.2.1. Test setup

Tensile tests under monotonic loading are carried out at ambient temperature and following the guidelines given by ASTM D3039/D3039M-14 [39]. A constant head displacement rate of 2 mm/min is applied. This strain rate is selected to produce failure within 1 to 10

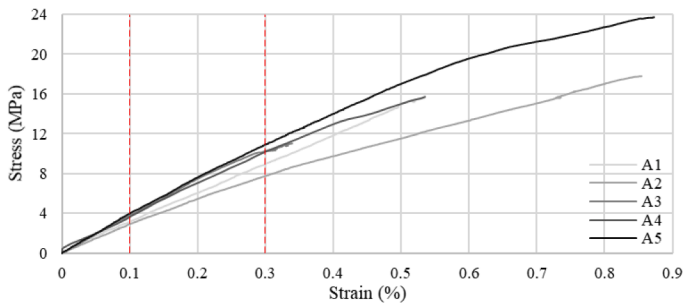

Fig. 11. Stress vs. strain curves of specimens A1-A5 under monotonic tensile tests at 25 °C.

Table 3
Uniaxial tensile test results (25 °C).

Specimen	Modulus (MPa)	Ultimate load (kN)	Ultimate extension (mm)	Ultimate stress (MPa)	Ultimate strain (%)
A1	2900	10.8	0.442	15.6	0.55
A2	2420	13.9	0.691	17.8	0.85
A3	3260	8.0	0.276	11.1	0.34
A4	3260	11.9	0.820	15.7	0.54
A5	3462	17.9	0.708	23.2	0.87
Average	3100	12.5	0.587	16.7	0.63

minutes. The tensile test setup is shown in Fig. 10. All tensile tests including constant and cyclic displacement loading rate, have been carried out on a 50 kN Instron that is equipped with a non-contact video extensometer (AVE2) to monitor the extension between the two black markers shown in Fig. 10.

3.2.2. Test results

Fig. 11 shows the stress vs. strain curves for five specimens (A1-A5) tested under monotonic tensile loading at ambient temperature. The elastic modulus is computed through the chord modulus (Eq. 1) taken in the strain range 0.1% to 0.3% [39] as indicated by red dashed lines.

$$E^{chord} = \frac{\Delta\sigma}{\Delta\varepsilon} 1$$

E^{chord} is the tensile chord modulus of elasticity, $\Delta\sigma$ is the stress difference and $\Delta\varepsilon$ the strain difference in the range 0.1% to 0.3%.

Tensile test results under monotonic loading are given in Table 3. The average elastic modulus is 3100 MPa. The ultimate tensile load and extension are 12.5 kN and 0.587 mm, respectively. The ultimate stress and strain are 16.7 MPa and 0.63%, respectively.

Two failure modes have been observed. In the first failure mode (A1), shown in Fig. 12a, one of the legs of the SMP core breaks and the aluminum tube slides out. In the second failure mode (A2 to A5), shown in Fig. 12b, the aluminum tube slides out without any breakage of the core. The difference between the two failure modes depends on the ratio between the SMP core strength and the bond strength between the core and aluminum tubes. However, this has no obvious impact on the strength of the connection since specimen A1 falls within the average level among the test results (see Fig. 11). In both failure modes, the SMP-aramid skin does not break, therefore adding more layers of aramid fabric to increase the thickness of the reinforcement skin will give little to no extra benefit to the strength of the connection at ambient temperature (25 °C).

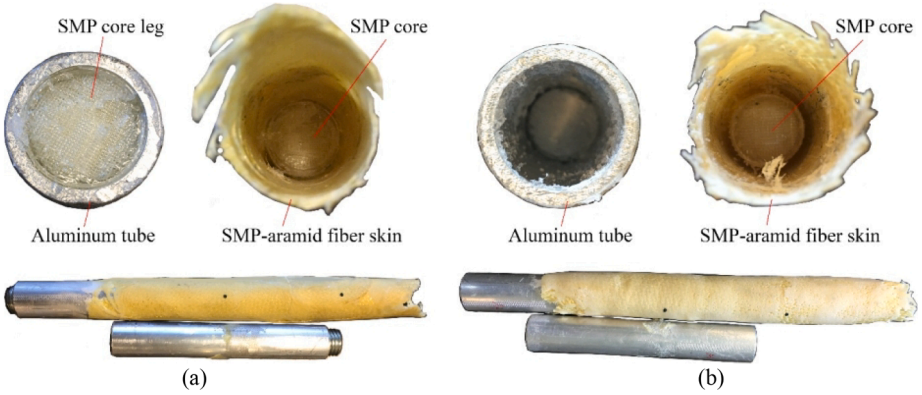

Fig. 12. Two failure modes (a) and (b) under monotonic tensile test at 25 °C.

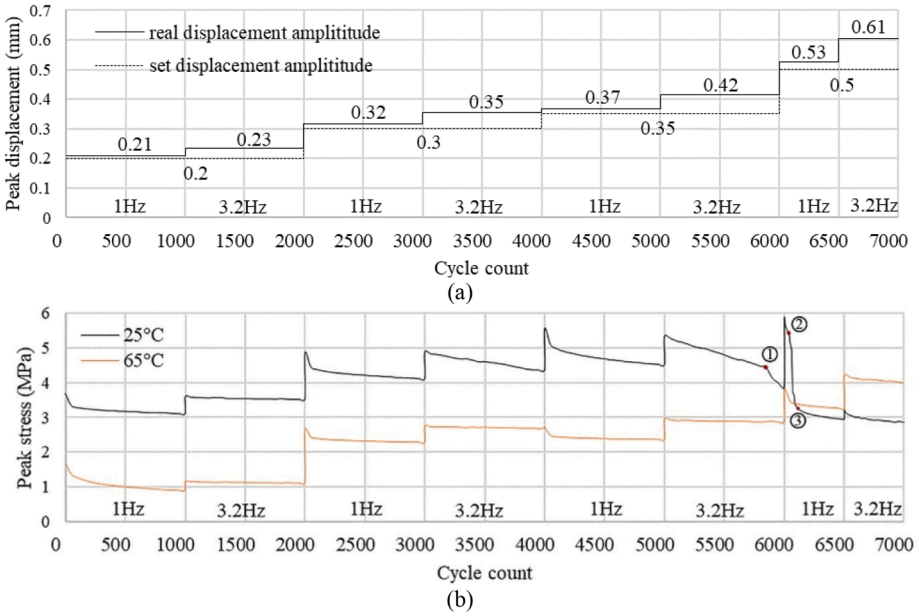

Fig. 13. Cyclic tensile tests: (a) comparison of measured and set displacement amplitudes vs. cycle count; (b) peak stress vs. cycle count curves for specimens D1(25 °C) and D2(65 °C).

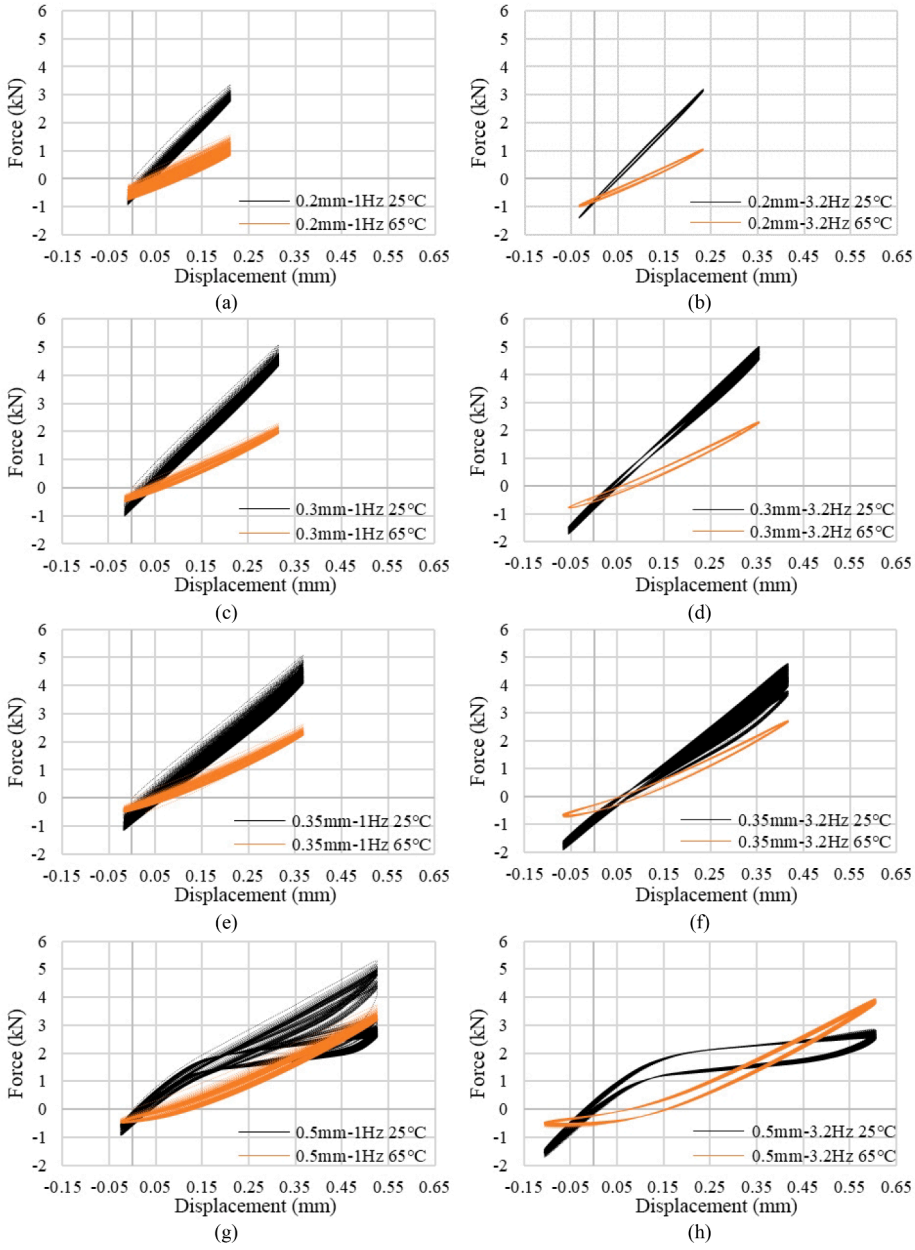

Fig. 14. Force vs. displacement curves for specimens D1 (25 °C) and D2 (65 °C) under 1 Hz and 3.2 Hz cyclic tensile loading with set displacement amplitudes of 0.2 mm, 0.3 mm, 0.35 mm, and 0.5 mm.

3.3. Cyclic tensile test, uncontrolled (25 °C) vs. controlled (65 °C)

3.3.1. Test setup

Cyclic tensile tests are carried out by controlling the displacement (strain) applied to the specimen within a set amplitude. Each cycle of the test includes a loading and unloading process. The average ultimate extension obtained from monotonic tensile tests (Section 3.2.2) is 0.587 mm. The amplitude of the cyclic displacement ranges from 30% to 80% of the ultimate extension. Considering typical loading scenarios for civil structures, the response is likely to be dominated by the 1st mode. For this reason, a testing frequency of 3.2 Hz is chosen because it is close to the 1st mode frequency of the three-story frame prototype (see Fig. 8b). For each test, 1000 displacement cycles are performed at a frequency of 1 Hz and 3.2 Hz, respectively, for a total of 2000 cycles for each applied displacement.

The displacement amplitude is first set to 0.2 mm, and then it is increased to 0.3, 0.35 and 0.5 mm. The test continues until the specimen breaks. After a first damage event occurs, extra 500 cycles are carried out at a loading rate of 1 Hz and 3.2 Hz, respectively.

Two specimens D1 and D2 have been tested: D1 core is tested at ambient temperature (uncontrolled case at 25 °C), while D2 core is actuated to the transition temperature (controlled case at 65 °C). The test setup for D1 and D2 is shown in Fig. 10 (a) and (b), respectively.

3.3.2. Test results

Fig. 13a shows the plot of the cyclic loading procedure which applies to both D1 (25 °C) and D2 (65 °C). The dashed and continuous lines indicate the set and measured displacement amplitude, respectively. The measured displacement amplitudes are marginally larger than the set values because of the tester overshooting. The displacement overshooting at 3.2 Hz is larger than that at 1 Hz, however, in both cases the overshooting is marginal. Under 0.2, 0.3, and 0.35 mm set displacement, 1000 cycles are carried out at a frequency of 1 Hz and 3.2 Hz, respectively. Since damage develops after testing under 0.35 mm set

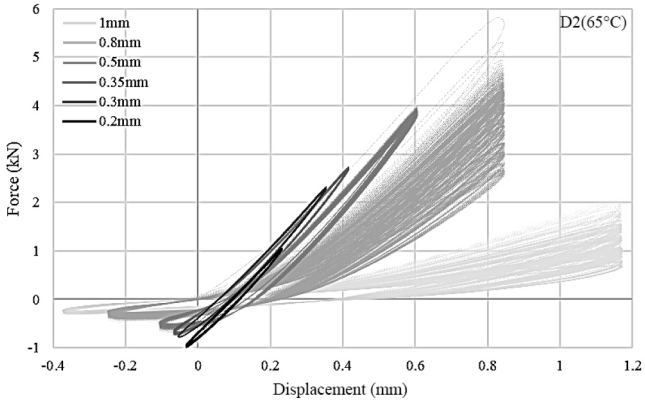

Fig. 15. Force vs. displacement curves for specimen D2 (65 °C) under cyclic tensile tests.

displacement, only 500 cycles are carried out at 1 Hz and 3.2 Hz, respectively, under 0.5 mm set displacement.

Fig. 13b shows the plots of peak stress and displacement over the cycle count. The black and orange curves indicate results for D1 (25 °C) and D2 (65 °C), respectively. Generally, a stepwise increment of the applied displacement causes a steep increase in peak stress which is followed by a rapid decay in the first 10 to 50 cycles. Subsequently, the peak stress decreases marginally in the remaining part of the 1000-cycle range. This decrease in peak stress is attributed to fatigue effects due to the formation and development of microcracks. Damage development is particularly evident when the applied displacement is increased stepwise, which is followed by a pronounced peak stress drop and a subsequent stabilization. It can be observed that the slope of the curves remains similar within each 1000-cycle range after the displacement amplitude is increased stepwise.

Referring to D1 (25 °C), in the first 5000 cycles no obvious damage occurs. In the 5000–6000 cycle range, peak stress suddenly decreases (point 1) because significant damage occurs at cycle 5870. The sudden increase of peak stress after the 6000th cycle is caused by a change of displacement from 0.35 to 0.5 mm. However, the peak stress drops rapidly after point 2 because damage develops further. After point 3, the peak stress stabilizes at approximately 3 MPa. The specimen can still carry tensile loading. Referring to D2 (65 °C), in the first 5000 cycles, the change of peak stress is similar to that for D1. Generally, a step-wise increment of the applied displacement causes a steep increase in peak stress. Notable is the decrease in peak stress that occurs across the 4000th cycle when the displacement amplitude is increased from 0.35 to 0.37 mm (see Fig. 13a). Since the displacement amplitude does not increase much, the step down in frequency and the associated drop in modulus causes the peak stress to decrease instead of increasing, i.e. frequency-dependent viscoelastic effects are dominant. For subsequent series of cycles in the range 5000–6000, no significant damage developments are observed.

Fig. 14 plots the force–displacement curves for D1 (25 °C) and D2 (65 °C). The large spread that characterizes the 1 Hz force–displacement curves is caused by the gradual drop in peak stress due to fatigue effects. This is the same effect observed in Fig. 13. Most microcrack-related damage occurs and develops within the first 100 cycles after the stepwise increase in displacement amplitude, which is always performed first at 1 Hz. Negative values are recorded for the force because the specimen undergoes permanent extension due to damage development, hence when the tester returns to the zero set position, it puts the specimen under compression. The occurrence and development of larger damage in D1 (macro cracks and delamination) can be observed from the change of slope of the force–displacement curves (black) from Fig. 14f ~ h, which shows progressively larger hysteresis loops as energy is dissipated through friction generated by the sliding movements of broken fibers and delaminated surfaces.

Since no major damage has occurred in D2 (65 °C), extra cyclic tests are performed by setting the displacement amplitude to 0.8 and 1.0 mm at a frequency of 3.2 Hz. Fig. 15 shows the plot of force vs. displacement curves of all applied displacement amplitudes. Under an applied displacement of 0.2, 0.3, 0.35, and 0.5 mm, the force vs. displacement curves feature hysteresis loops due to viscoelastic effects. When the set displacement amplitude increases to 0.8 mm (measured value 0.84 mm), significant damage starts to develop as indicated by the drop in peak stress that occurs over the cycles. Similar results are recorded under 1 mm set displacement (measured value 1.17 mm). Note that the average force is smaller than that recorded under an applied displacement of 0.8 mm due to damage.

For specimen D1 (25 °C), damage starts to develop from the 5870th cycle under a set displacement of 0.35 mm (actual value 0.42 mm), which is 72% of the ultimate tensile extension (see Section 3.2.2). The maximum force and stress for D1 (25 °C) during cyclic tensile testing are approximately 5.3 kN and 6 MPa that are 42% and 26% of the ultimate tensile load and stress, respectively. For specimen D2 (65 °C), damage starts to develop from the 7000th cycle under a set displacement of 0.8 mm (actual value 0.84 mm). The maximum force and stress for D2 (65 °C) reach up to approximately 5.7 kN and 4 MPa that are 46% and 24% of the ultimate tensile load and stress, respectively. Through actuation of the joint core, the specimen becomes more ductile. However, the specimen stiffness decreases by approximately half because of the stiffness reduction of the core.

A subsequent monotonic tensile test is carried out on specimen D1 (25 °C) during which the tube element slides out without obvious damage in the core as shown in Fig. 16a. For specimen D2 (65 °C), the tube elements do not slide out under a subsequent monotonic tensile test. However, the specimen features extended damage as can be inferred from the broken skin fibers and the large extensional deformation that is indicated in Fig. 16b. This means that when the joints are thermally actuated to the transition temperature, the core stiffness reduction causes a significant weakening. As expected, the load is taken primarily

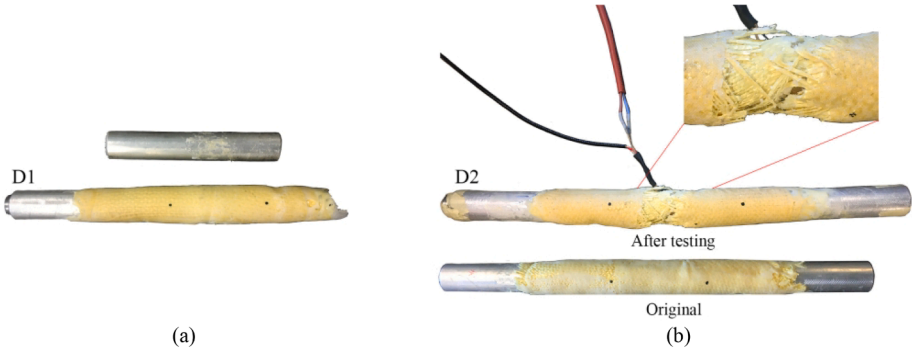

Fig. 16. Failure of (a) D1(25 °C) and (b) D2(65 °C) specimens under monotonic tensile test carried out after cyclic tensile tests.

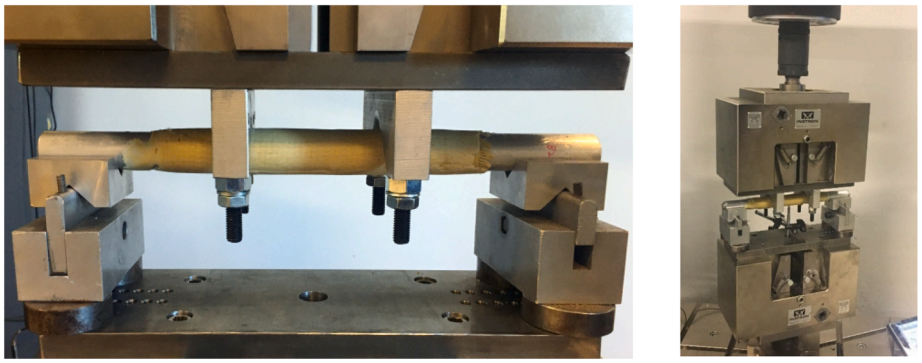

Fig. 17. Four-point bending test setup at 25 °C.

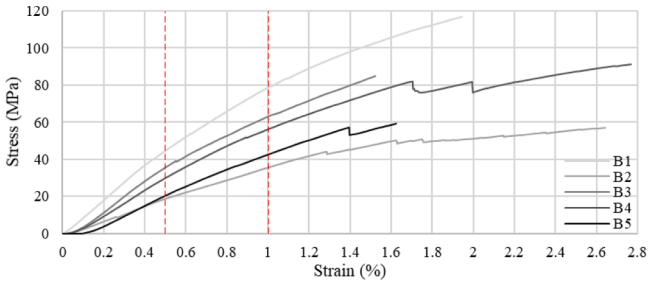

Fig. 18. Stress vs. strain curves for specimens B1-B5 under four-point bending test at 25 °C.

by the reinforcement skin. Therefore, adding more layers of aramid fabric would be beneficial to mitigate the weakening caused by the core stiffness reduction.

4. Monotonic and cyclic bending test on joint-element connection

4.1. Monotonic four-point bending test (25 °C)

4.1.1. Test setup

Monotonic four-point bending tests are carried out at ambient temperature (25 °C) following the guidelines given in ASTM 6272–02 [40]. Tests are performed using a 50 kN Instron tester. The test setup is shown in Fig. 17. The specimen lies on two supports and is loaded at two points. The span between the two loading noses (i.e. the load span) is 100 mm that is one-third of the support span (300 mm). A constant head displacement rate of 5 mm/min is applied. The vertical displacement is measured directly through the actuator stroke position feedback of the Instron tester.

4.1.2. Test results

The maximum stress occurs in the outer fibers within the load span. The flexural stress σ^f , strain ε^f and modulus E^f for cylindrical specimens are calculated from Eqs. 2 ~ 4 [40] , respectively.

$$\sigma^f = \frac{8LS_S(1-\frac{S_L}{S_S})}{\pi D^3} \quad 2$$

$$\varepsilon^f = \frac{12dD}{{S_S}^2(3-(1-\frac{S_L}{S_S})^2} \quad 3$$

$$E^f = \frac{\Delta\sigma^f}{\Delta\varepsilon^f} \quad 4$$

where L is the load; S_S is the support span; S_L is the load span; D is the diameter of the specimen; d the measured deflection; $\Delta\sigma^f$ and $\Delta\varepsilon^f$ are the flexural stress and strain difference, respectively, between the two loading points.

Fig. 18 shows the plot of flexural stress vs. strain curves for five specimens B1-B5. The flexural modulus is computed through the chord modulus (Eq. 4) between the strain range 0.5% to 1% that is indicated by red dashed lines.

Table 4
Four-point bending test results (25 °C).

Specimen	Flexural modulus (MPa)	Ultimate load (kN)	Ultimate deflection (mm)	Ultimate flexure stress (MPa)	Ultimate flexure strain (%)
B1	6811	6.17	12.5	116.7	1.95
B2	3351	3.45	16.1	56.9	2.64
B3	5494	4.79	9.5	84.9	1.52
B4	5249	5.69	16.7	91.0	2.77
B5	4448	3.94	9.6	59.2	1.62
Average	5070	4.81	12.9	81.8	2.10

Bending test results under monotonic loading are given in Table 4. The average flexural modulus is 5070 MPa. The ultimate flexural load and deflection are 4.81 kN and 12.9 mm, respectively. The ultimate flexural stress and strain are 81.8 MPa and 2.1%, respectively.

Fig. 19 shows an example of the failure mode under bending for specimen B2. The outer fibers at the tension direction of the reinforcement skin break first, followed by load transfer to the core that breaks subsequently. This failure mode suggests that adding more layers of aramid fabric could improve the flexural strength of the joint-element connection. Note that the measured flexural modulus (average 5070 MPa) is 2/3 times higher than that measured from uniaxial tension (average 3100 MPa). The difference in tensile and flexural modulus is due to the effect of the stiff reinforcement skin which greatly improves the flexural stiffness.

4.2. Cyclic tensile test (25 °C vs. 65 °C)

4.2.1. Test setup

Two specimens are tested under cycling bending loading: D3 is tested at ambient temperature (25 °C) while D4 core is thermally actuated to 65 °C. Different from cyclic tensile testing, only 1 Hz frequency is tested under bending. The 1st mode shape of the prototype frame shown in Fig. 8b is characterized by a lateral sway that mostly causes reversal of tension/compression forces in the structural elements. Therefore, cycling bending testing performed at the 1st natural frequency is not of particular interest.

The test setup for D3 is identical to that for specimens B1-B5. Fig. 20a shows the four-point bending test setup for specimen D4 (65 °C). Fig. 20b is taken by a thermal camera when the joint core is actuated to 65 °C.

4.2.2. Test results

The specimens are tested for 1000 cycles under a set displacement amplitude of 2, 3, 4 mm followed by 500 cycles carried out under a set displacement amplitude of 5 mm. All tests are carried out at a frequency of 1 Hz. Due to the tester overshooting, the measured displacement

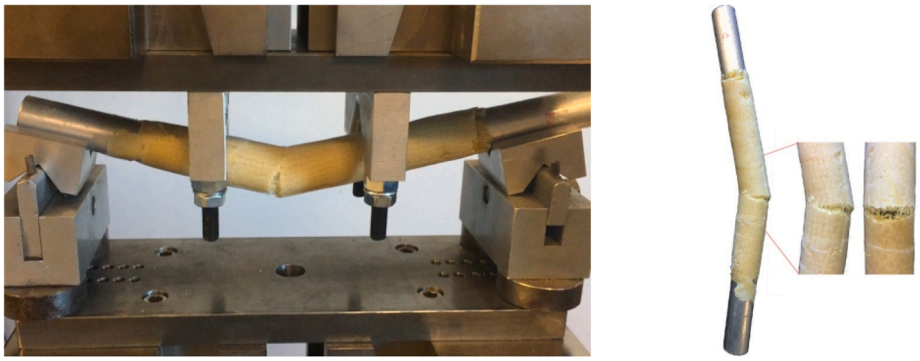

Fig. 19. Specimen B2 failure under four-point bending test at 25 °C.

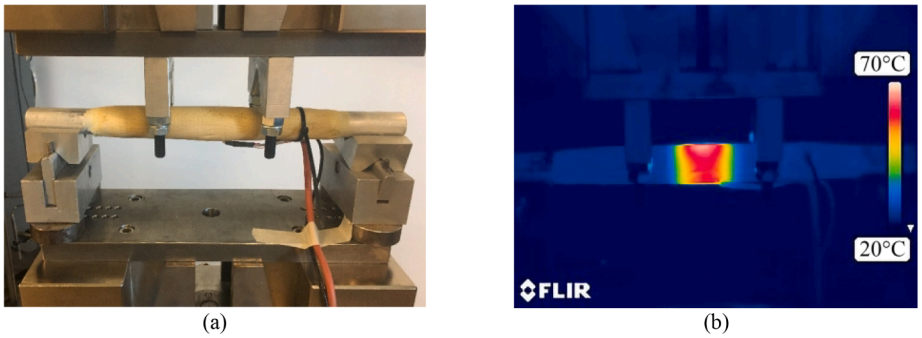

(a) (b)

Fig. 20. (a) four-point bending test setup for specimen D4 (65 °C); (b) joint core temperature distribution.

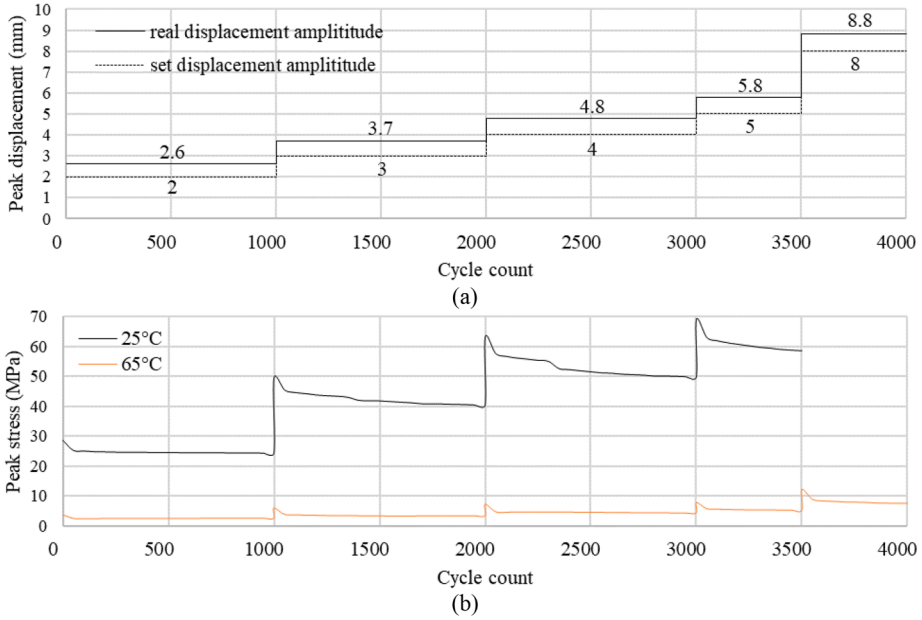

Fig. 21. Cyclic bending tests: (a) comparison of measured and set displacement amplitudes vs. cycle count; (b) peak stress vs. cycle count curves for specimens D3 (25 °C) and D4(65 °C).

amplitudes are 2.6, 3.7, 4.8, and 5.8 mm. Fig. 21 shows the plots of peak stress and displacement over the cycle count. The peak stress has similar behavior to what has been observed during tensile testing. A stepwise increment of the applied displacement causes a steep increase in peak stress which is followed by a gradual drop caused by fatigue effects (microcracks development). This explains the spread that characterizes the force vs displacement curves that are shown in Fig. 22 for D3 (25 °C, black curves) and D4 (65 °C, orange curves).

Referring to D3 (25 °C), a significant change in the force vs. displacement curves can be observed from the 305th cycle under an applied displacement amplitude of 4 mm, which indicates damage development, Fig. 22c. This damage is caused by the rupture of some of the skin fibers. When the loading amplitude increases to 5 mm, there is a slight increase in the measured force because of load transfer from the broken fibers to other fibers in the skin. Increasing the displacement amplitude further to 5 mm (5.8 mm measured displacement), causes

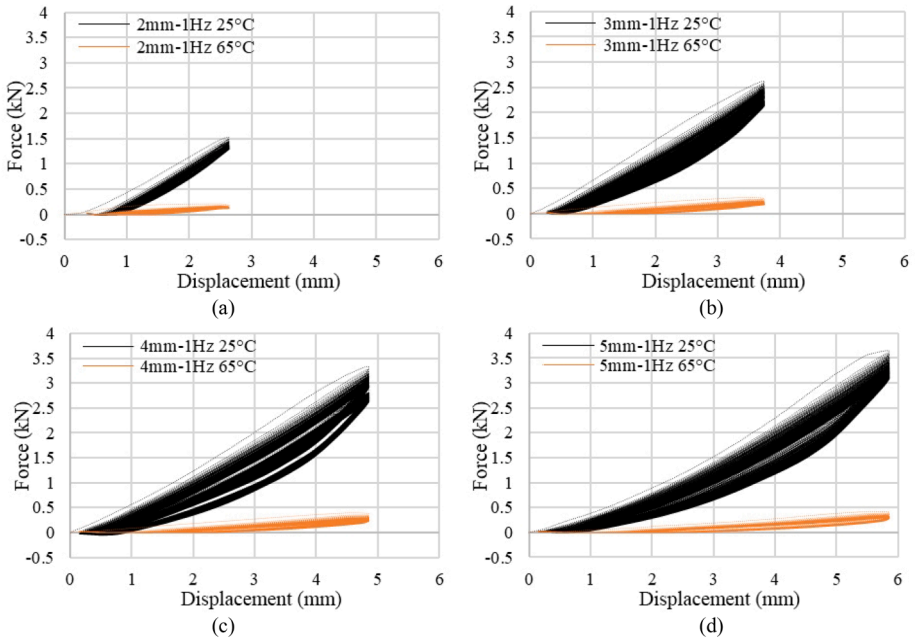

Fig. 22. Force vs. displacement curves for specimens D3 (25 °C) and D4 (65 °C) under 1 Hz bending loading with set displacement amplitudes of (a) 2 mm, (b) 3 mm, (c) 4 mm, and (d) 5 mm.

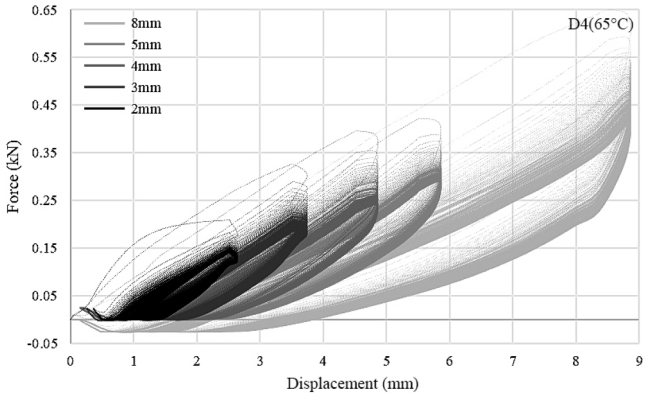

Fig. 23. Force vs. displacement curves of specimen D4(65 °C) under cyclic bending tests.

more skin fibers to break which leads to the core failure. The failure mode under cyclic bending tests is similar to the failure mode under monotonic bending tests shown in Fig. 19.

Referring to D4 (65 °C), the average bending stiffness reduces dramatically (up to 90%) owing to thermal actuation of the core, which can be thought of as a transition from moment connection before actuation to pin connection after actuation. No obvious damage has been observed.

For clarity, D4 force–displacement curves under an applied displacement of 2, 3, 4, 5 mm are plotted in Fig. 23. An extra test is carried out with a set displacement of 8 mm. When the applied displacement amplitude is increased to 8 mm, the hysteresis loop area increases significantly. Although no obvious damage can be observed in the specimen from Fig. 23, the deformation is very pronounced. Fig. 24 shows that the tested specimen is considerably bent, the core largely deformed, and the skin fibers are wrinkled. However, the core and fibers are not broken and the core can be bent back into its original shape after heating again to the transition temperature.

5. Discussion

This paper has focused on component-level testing to investigate the mechanical properties of a new semi-active vibration control device that comprises an SMP core reinforced by an SMP-aramid skin. This control device also functions as a load-transfer component in the form of a joint. The mechanical properties of the joint-element connection have been

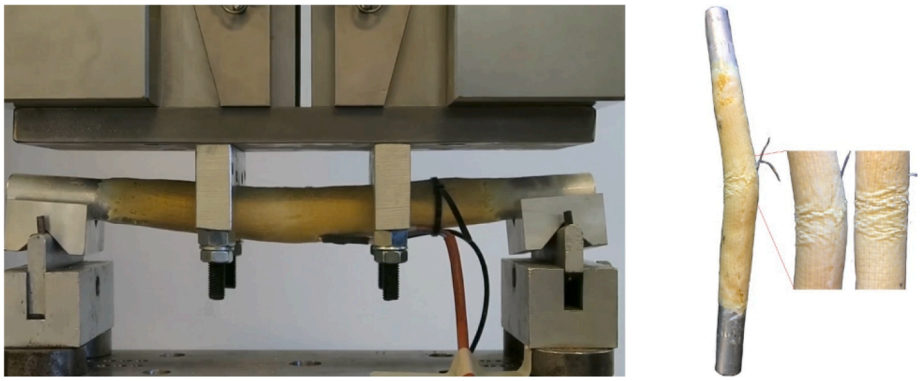

Fig. 24. Specimen D4 (65 °C) after cyclic bending tests.

evaluated through tensile and bending tests under monotonic and cyclic loading.

From monotonic tensile tests, an average elastic modulus of 3100 MPa has been measured. The ultimate tensile load and extension are 12.5 kN and 0.587 mm, respectively. The ultimate stress and strain are 16.7 MPa and 0.63%, respectively. Failure occurs as the aluminum tubes slide out from the SMP-aramid skin. However, the reinforcement skin fibers do not break. Therefore, adding more layers of aramid fabric will give little to no extra benefit to the connection strength. The tensile strength of the joint-element connection depends mostly on the strength of the bond between the SMP-aramid skin and the aluminum tube. To achieve a stronger connection, the SMP-aramid skin could cover a larger area of the connecting elements, and a stronger structural glue could be applied in between the joint core and the tubes. In addition, clamping the skin and tube together may be beneficial.

From monotonic four-point bending tests, an average bending modulus of 5070 MPa has been measured. The ultimate flexural load and extension are 4.81 kN and 12.9 mm, respectively. The ultimate flexural stress and strain are 81.8 MPa and 2.1%, respectively. After testing, all specimens feature damage caused by breakage of the outer fibers within the load span. The outer fibers along the tension direction of the reinforcement skin have broken sequentially. The core fails immediately after all outer fibers break. Therefore, adding more layers of aramid fabric can effectively improve the bending strength of the joint-element connection.

From the cyclic tests under both tensile and bending loading, it has been observed that when the joint core is actuated to the transition temperature, material viscoelasticity is beneficial for increasing ductility and energy dissipation. Under cycling tensile loading, the core stiffness reduction causes a significant weakening in the middle of the specimen. The specimen features extended damage caused by breakage of the skin fibers, which leads to large extensional deformation. Since the load is taken primarily by the reinforcement skin, adding more layers of aramid fabric would be beneficial to mitigate the weakening caused by the core stiffness reduction. Through thermal actuation of the joint core, bending stiffness reduces by up to 90%. This can be thought of as the effect of releasing rotational degrees of freedom from a moment connection as the joint transitions to a pin connection. Core and fibers do not break even after undergoing large deformations caused by cycling bending testing.

6. Conclusion

Adaptive components make use of the viscoelastic properties of SMP to change the dynamic characteristics of the structure in which they are embodied. Thermal actuation of the component core material to the transition range causes a reduction of stiffness and an increase in material damping. At the structure level, the change of the component mechanical property causes a shift of the natural frequencies and an increase of the structural damping ratio, which has been successfully employed for semi-active vibration control.

Testing carried out at the component level has given important insights into the mechanical properties of the joint-element connection. While increasing damping and ductility, thermal actuation also reduces tensile and bending strength. To limit this effect, increasing the thickness of the reinforcement skin, by adding more layers of aramid fabric, will be beneficial to both tensile and bending strength. To improve the overall strength of the joint-element connection, a different type of load-transfer mechanism could be tested which does not rely on the bond strength between the SMP-aramid skin and the connecting elements. The specimens that have been tested have dimensions that relate to the 1/10 scale prototype frame described in Section 2.2. To investigate scaling effects, components of larger size could be tested.

At the structure level, shake table tests have been carried out on a 1/10 scale three-story frame prototype equipped with twelve adaptive joints. The tests carried out in this work confirm previous findings. Results have shown that semi-active control through thermal actuation of variable stiffness and damping components is effective to mitigate the response under resonance and earthquake loadings. In resonance conditions, top-story acceleration and base shear are reduced by up to 76% and 85%, respectively, while depending on the earthquake type, reduction in the range 43–54% for top-story acceleration and 35–67% for base shear have been experimentally measured.

Future work could also investigate the application of variable stiffness components for structural adaptation to loading through shape control [5]. Shape control of truss and frame structures is typically performed through length changes of linear actuators that are fitted on the structural elements. Depending on the joint type, a change of shape might cause stress build-ups. If the structure is equipped with adaptive joints, thermal actuation could be performed in parallel to linear actuation so to cause a significant decrease in bending stiffness which will reduce stress build-ups and the energy required for adaptation to loading through shape control.

7. Data availability

All data generated for this study are included in the article.

CRediT authorship contribution statement

Qinyu Wang: Conceptualization, Data curation, Formal analysis, Investigation, Methodology, Writing – original draft, Writing – review & editing. **Gennaro Senatore:** Conceptualization, Methodology, Validation, Supervision, Writing – review & editing. **Kaspar Jansen:** Methodology, Validation, Supervision, Writing – review & editing. **Arjan Habraken:** Supervision. **Patrick Teuffel:** Project administration, Supervision.

Declaration of Competing Interest

The authors declare that they have no known competing financial interests or personal relationships that could have appeared to influence the work reported in this paper.

Acknowledgments

This research project “Adaptive Joints with Variable Stiffness” has been supported by 4TU Lighthouse Projects 2017 (LHP2017) and China Scholarship Council (CSC).

References

[1] Teuffel P. “Entwerfen Adaptiver Strukturen,” (Doctoral dissertation), University of Stuttgart - ILEK, Struttgart, 2004.
[2] Sobek W. Ultra-lightweight construction. Int J Space Struct 2016;31(1):74–80.
[3] Senatore G, Duffour P, Winslow P. Synthesis of Minimum Energy Adaptive Structures. Struct Multidiscip Optim 2019;60(3):849–77. https://doi.org/10.1007/s00158-019-02224-8.
[4] Wang Y, Senatore G. Minimum energy adaptive structures - All-In-One problem formulation. Comput Struct 2020;236:106266. https://doi.org/10.1016/j.compstruc.2020.106266.
[5] Reksowardojo AP, Senatore G, Smith IFC. Design of structures that adapt to loads through large shape changes. J. Struct. Eng. (ASCE) 2020;146(5):04020068. https://doi.org/10.1061/(ASCE)ST.1943-541X.0002604.
[6] Senatore G, Reksowardojo AP. Force and shape control strategies for minimum energy adaptive structures. Front Built Environ 2020;6(105). https://doi.org/10.3389/fbuil.2020.00105.
[7] Reksowardojo AP, Senatore G, Smith IFC. Experimental testing of a small-scale truss beam that adapts to loads through large shape changes. Front Built Environ 2019;5(93). https://doi.org/10.3389/fbuil.2019.00093.
[8] Ghaedi K, Ibrahim Z, Adeli H, Javanmardi A. Invited Review: Recent developments in vibration control of building and bridge structures. J Vibroeng 2017;19(5):3564–80.
[9] Thenozhi S, Yu W. Advances in modeling and vibration control of building structures. Ann Rev Cont 2013;37(2):346–64.
[10] Soong TT, Spencer BF. Active, semi-active and hybrid control of structures. Bull New Zealand Soc Earthquake Eng 2000;33(3):387–402.

[11] Kandasamy R, Cui F, Townsend N, Foo CC, Guo J, Shenoi A, et al. A review of vibration control methods for marine offshore structures. Ocean Eng 2016;127:279–97.
[12] Spencer BF, Nagarajaiah S. State of the art of structural control. J Struct Eng 2003;129(7):845–56.
[13] Huang B, Zhang H, Wang H, Song G. Passive base isolation with superelastic nitinol SMA helical springs. Smart Materials and Structures. Smart Mater Struct 2014;23(6):065009.
[14] Kasai K, Fu Y, Watanabe A. Passive control systems for seismic damage mitigation. J Struct Eng 1998;124(5):501–12.
[15] Chang CC. Mass dampers and their optimal designs for building vibration control. Eng Struct 1999;21(5):454–63.
[16] Chang JC, Soong TT. Structural control using active tuned mass dampers. J Eng Mech Div 1980;106(6):1091–8.
[17] Weidner S, Kelleter C, Sternberg P, Haase W, Geiger F, Burghardt T, et al. The implementation of adaptive elements into an experimental high-rise building. Steel Constr: Des Res 2018;11(2):109–17.
[18] Wang L, Wang X, Li Y, Lin G, Qiu Z. Structural time-dependent reliability assessment of the vibration active control system with unknown-but-bounded uncertainties. Struct Contr Health Monitor 2017;24(10):e1965. https://doi.org/10.1002/stc.1965.
[19] Symans MD, Constantinou MC. Semi-active control systems for seismic protection of structures: a state-of-the-art review. Eng Struct 1999;21(6):469–87.
[20] Zhao Y-L, Xu Z-D, Wang C. Wind vibration control of stay cables using magnetorheological dampers under optimal equivalent control algorithm. J Sound Vib 2019;443:732–47.
[21] Kınay G, Turan G. A hybrid control of seismic response by passive and semi-active control strategies. Journal of Engineering Science and Design 2012;2(1):27–36.
[22] Spencer BF, Sain MK. Controlling buildings: a new frontier in feedback. IEEE Control Syst Mag 1997;17(6):19–35.
[23] Gkatzogias KI, Kappos AJ. Semi-active control systems in bridge engineering: a review of the current state of practice. Struct Eng Int 2016;26(4):290–300.
[24] Kobori T, Takahashi M, Nasu T, Niwa N, Ogasawara K. Seismic response controlled structure with Active Variable Stiffness system. Earthquake Eng Struct Dyn 1993;22(11):925–41.
[25] Sarlis AA, Pasala DTR, Constantinou MC, Reinhorn AM, Nagarajaiah S, Taylor DP. Negative Stiffness Device for Seismic Protection of Structures. J Struct Eng 2013;139(7).
[26] Shu Z, Zhang J, Nagarajaiah S. Dimensional Analysis of Inelastic Structures with Negative Stiffness and Supplemental Damping Devices. J Struct Eng 2017;143(3).
[27] Wang Q, Senatore G, Jansen K, Habraken A, Teuffel P. Design and characterization of variable stiffness structural joints. Mater Des 2020;187:108353. https://doi.org/10.1016/j.matdes.2019.108353.
[28] Wang Q, Senatore G, Jansen K, Habraken A, Teuffel P. Vibration suppression through variable stiffness and damping structural joints. Front Built Environ 2020;6. https://doi.org/10.3389/fbuil.2020.550864.
[29] Wang Q, Senatore G, Jansen K, Habraken A, Teuffel P. Seismic control performance of a three-story frame prototype equipped with semi-active variable stiffness and damping structural joints. Earthquake Eng Struct Dyn 2021;50(13):3379–402. https://doi.org/10.1002/eqe.3514.
[30] Huang WM, Yang B, Fu YQ. Polyurethane shape memory polymers. CRC Press; 2011.
[31] Hu J, Chen W, Fan P, Gao J, Fang G, Cao Z, et al. Epoxy shape memory polymer (SMP): Material preparation, uniaxial tensile tests and dynamic mechanical analysis. Polym Test 2017;62:335–41.
[32] Huang WM, Yang B, Zhao Y, Ding Z. Thermo-moisture responsive polyurethane shape-memory polymer and composites: a review. J Mater Chem 2010;20(17):3367–81.
[33] Menard KP. Dynamic mechanical analysis : a practical introduction. Boca Raton: CRC Press; 2008.
[34] ISO-6721-1, "Plastics Determination of dynamic mechanical properties - ISO 6721-1," ISO, Geneva, 2011.
[35] Hardy JG, Palma M, Wind SJ, Biggs MJ. Responsive biomaterials: advances in materials based on shape-memory polymers. Adv Mater 2016;28(27):5717–24.
[36] Liu Y, Du H, Liu L, Leng J. Shape memory polymers and their composites in aerospace applications: a review. Prog Mater Sci 2011;56(7):1077–135.
[37] Gall K, Mikulas M, Munshi NA, Beavers F, Tupper M. Carbon fiber reinforced shape memory polymer composites. J Intell Mater Syst Struct 2000;11(11):877–86.
[38] Santhosh Kumar KS, Khatwa AK, Reghunadhan Nair CP. High transition temperature shape memory polymers (SMPs) by telechelic oligomer approach. React Funct Polym 2014;78:7–13.
[39] A. S. T. M. Standard, "D3039/D3039M-14," *Standard test method for tensile properties of polymer matrix composite materials,* 2014.
[40] A. S. T. M. Standard, "D6272," *Standard test method for flexural properties of unreinforced and reinforced plastics and electrical insulating materials by four-point bending,* 2002.